




# Comparative studies of CdS thin films by chemical bath deposition techniques as a buffer layer for solar cell applications

A. Ashok<sup>1</sup> · G. Regmi<sup>1</sup> · A. Romero-Núñez<sup>1</sup> · M. Solis-López<sup>1</sup> · S. Velumani<sup>1,2</sup>  · H. Castaneda<sup>2</sup>

Received: 21 October 2019 / Accepted: 30 January 2020 / Published online: 14 February 2020  
© Springer Science+Business Media, LLC, part of Springer Nature 2020

## Abstract

Cadmium sulfide (CdS) buffer layer that decouples the absorber layer and window layer in thin-film solar cells was synthesized by two different chemical bath deposition (CBD) techniques with varying deposition parameters. X-ray diffraction (XRD) revealed that the CdS thin film crystallizes in a stable hexagonal wurtzite structure having a preferential orientation along (002) reflection plane with a crystallite size varying from 20 to 40 nm. First longitudinal optical phonon mode was identified at Raman shift of  $305\text{ cm}^{-1}$ . Uniform, granular, continuous, and smooth surface with an average grain sizes ( $< 100\text{ nm}$ ) as well as small roughness ( $< 9\text{ nm}$ ) was observed by scanning electron microscopy (SEM) and atomic force microscopy (AFM), respectively. The symmetric composition of cadmium and sulfur along with larger grains (20 nm) was observed at higher deposition temperatures and times. The optical band gap of CdS samples obtained from process one was in the range of 2.3–2.35 eV, while the band gap by the second CBD process lay in between 2.49 and 2.65 eV, showing the most stable compound of CdS. The presence of a green emission band in photoluminescence spectra (PL) demonstrated that the CdS material has better crystallinity with minimum defect density. Hall effect studies revealed the n-type conductivity of CdS thin films with a carrier concentration values in the order of  $10^{16}\text{ cm}^{-3}$ . Furthermore, CdS thin films fabricated by CBD process exposed better quality that might be more suitable material as a buffer layer for thin-film solar cells.

## 1 Introduction

Historically, energy production and its consumption have been a keystone factor in the development of human civilization. The consumption of energy is interconnected with world population growth as well as characteristics of modern society like life expectancy, mean years of schooling, water access, and electrification level etc. [1]. The world energy production is mainly achieved by burning fossil fuels. However, the use of fossil fuels has raised concerns due to its limited availability and environmental issues. The necessity to increase energy production for fulfilling the basic requirements without producing harmful gases becomes

one of the most challenging problems that our civilization must encounter. To have a scenario of constant growth in population with the equilibrium between good quality of life, the needs of energy production, proportional distribution of energetics and a non-threatened climate, the use of the clean renewable source of energy is an essential as a forward step that humanity has to take in the energy production evolution. If we consume the energy sources in a similar trend, it is necessary to remember that in a near-future these resources (non-renewable) start to run out not only leaving behind a hole in the energy harvest but also increase the price geometrically [2]. These will directly affect the entire population of the world qualitatively.

There is an acute worldwide concern to diminish the problems of the energy crisis and global warming due to greenhouse gas emissions mostly obtained from non-renewable fossil fuels through combustion [3]. Among different renewable energies (wind, hydropower, bioenergy, solar photovoltaic), the solar photovoltaic (PV) has achieved tremendous interest due to its most reliable, reliability, free availability with no pollution and fastest-growing market, by the fact that around 402 GW of total electricity generation capacity was installed by the end of 2017 and expected to reach 505 GW

✉ S. Velumani  
velu@cinvestav.mx

<sup>1</sup> Department of Electrical Engineering (SEES), Centro de Investigación y de Estudios Avanzados del IPN (CINVESTAV-IPN), Av. Instituto Politécnico Nacional 2508, C.P. 07360 Mexico City, Mexico

<sup>2</sup> Department of Materials Science and Engineering, National Corrosion and Materials Reliability Laboratory, Texas A&M University, Texas, USA

by the end of 2018 [4]. The solar energy is available in most of the areas around world and supplies an enormous source of energy that can easily cover world energy demand. Due to the continuous increase in the cell efficiency and the reduction in device fabrication cost, the solar cell is regarded as a spearhead in the research and development especially among other renewable energy sources. Depending upon the use of light-absorbing semiconductor material, PV technology can be divided into different generations, namely first, second, third, and fourth. Thin-film PV technology (hydrogenated a: Si, CdTe, CIGSe) belongs to the second-generation solar cell with some competitive advantages like much higher absorption coefficient ( $\alpha > 10^4 \text{ cm}^{-1}$ ) [5], longer operational lifetimes [6], higher stability and reliability [7], low cost [8], and higher efficiencies with much promise of getting better over other types of solar cells [9]. An essential part of these thin-film solar cells is the p-n junction or p-i-n junctions that convert sunlight directly into electricity. The p-n junctions of thin-film solar cells can be divided into heterojunction and homojunction depending on whether the semiconductor materials on one side of the junction are different or the same from that on the other side. If the incident photon energy is larger than that of the band gap of semiconductor, then semiconductor material absorbs solar energy, which generates the electron-hole pairs separated by the internal electric field of the junction. To allow the incident photon to the absorber layer effectively, the buffer material must have a large band gap, higher carrier density compared to absorber material, and very thin ( $\sim 50 \text{ nm}$ ) material to maintain low series resistance [10]. In this way, the photo-generation of charge carriers can be maximized with minimum recombination losses by the wider extension of the space charge region (SCR) into the absorber layer [11]. For this, there are several materials such as  $\text{In}_2\text{S}_3$ ,  $\text{In}_2\text{Se}_3$ ,  $\text{TiO}_2$ ,  $\text{In}(\text{OH})_3$ ,  $\text{ZnSe}$ ,  $(\text{Zn,Mg})\text{O}$ ,  $\text{InZnSe}_x$ ,  $\text{ZnO}$ ,  $\text{ZnS}$ , and  $\text{CdS}$  have been investigated as buffer materials for thin-film solar cells [12–19].

Semiconductor nanocrystals (NCs) have enough potential towards the attraction on various applications. Among them,  $\text{CdS}$  is the most promising material because of its enormous uses in optoelectronics [20], catalysis [21], gas sensors [22], optical filters [23], photodetectors [24], thin-film field effect transistors [25], semiconductor lasers [26], photo-electrochemical cells [27], and photovoltaics [28].  $\text{CdS}$  material has remained the preferred choice that attracted huge concern and interest from many researchers as it has egressed as one of the promising buffer materials for highly efficient polycrystalline thin-film-based solar cells ( $\text{CdTe}$ ,  $\text{CIGSe}$ ) [29–36]. The  $\text{CdS}$  thin films should have high transparency, not too thin to avoid short circuits and not too thick to prevent the light absorption in the buffer layer and low resistivity to improve the efficiency of solar cells [37]. The ultrathin  $\text{CdS}$  buffer layer couples the absorber material (i.e.,  $\text{CIGSe}$ ,  $\text{CdTe}$ ) and  $\text{ZnO}$  window layer in three main aspects, namely

electronically (band alignment), structurally (lattice match), and chemically (inter-diffusion) [38]. Besides the participation in the formation of the p-n junction, the  $\text{CdS}$  film also helps in the passivation of surface states of the  $\text{CIGSe}$  layer, mechanical protection from  $\text{ZnO}$  deposition, and elimination of surface oxides.  $\text{CdS}$  is a II–VI n-type semiconductor with a direct band gap of 2.38–2.58 eV and have wurtzite (stable,  $E_g = 2.58 \text{ eV}$ ) or cubic (metastable,  $E_g = 2.38 \text{ eV}$ ) crystal structures [39]. For high efficiency solar cells, a buffer layer with a hexagonal structure is preferred over the cubic one because of its higher optical band gap. The highly stable hexagonal phase invariably grows with columnar structure along the *c*-axis perpendicular to the substrate, introducing fewer grain boundaries parallel to the junction, which can impede the flow of photogenerated excess carriers to the grid [40]. The  $\text{CdS}$  thin-film material can be synthesized by a variety of fabrication techniques, divided into physical vapor deposition (PVD) and solution growth deposition techniques, such as sputtering [41, 42], evaporation [43, 44], molecular beam epitaxy (MBE) [45], sol-gel [46], electro-deposition [47, 48], screen printing [49], spin coating [50, 51], spray pyrolysis [52, 53], metal organic chemical vapor deposition (MOCVD) [54], successive ionic layer adsorption and reaction (SILAR) [55], close spaced sublimation [56], and chemical bath deposition (CBD) [57, 58]. Reynolds et al. [59] first discovered the photovoltaic effect by using  $\text{CdS}$  thin film with copper contact while studying the properties of different rectifying contacts to  $\text{CdS}$  crystal in 1954. The advantages and disadvantages of using various thin film deposition methods and the main parameters that can affect the properties of films are given in Table 1. Physical vapor deposition techniques typically operate at high temperatures and normally require higher capital costs. Solution growth deposition techniques offer opportunities to fabricate semiconductor compound material at lower temperatures and lower capital costs.

CBD is a solution growth process, which has been intensively applied for the research and industrial deposition of  $\text{CdS}$  thin films on different substrates because of its simplicity, low process temperature, scalability and reproducibility, high stability, low cost for large-scale production, and high device efficiency [60]. The first CBD method was reported in 1984 by synthesizing lead sulfide for photoconductive detectors [61]. In the CBD- $\text{CdS}$  growth process, there is a slow release of cadmium ions and sulfur ions and then condensation of these ions on the substrate in an aqueous alkaline bath solution giving adherent and uniform  $\text{CdS}$  thin films. The nucleation and growth of thin films deposited using CBD method can be influenced by parameters such as types of precursor material, the concentration of precursor material, bath temperature, time of deposition, solubility equilibrium, pH of the solution, speed of stirrer, and

**Table 1** Information of advantages, disadvantages, and parameters of CdS thin-film growth techniques [41–58]

S.N.	Growth methods	Advantages	Disadvantages	Main parameters
1.	Sputtering	Uniform, large area coverage, negligible impurities, etc.	High-cost equipment, high energy needed to operate	Base pressure, substrate temperature, sputter power, argon gas flow rate, time of deposition
2.	Evaporation	Controlled deposition rate, low contamination	Costly, more wastage of precursor material	Base pressure, source temperature, substrate temperature, time of deposition, precursor material
3.	Molecular beam epitaxy	High-purity elemental sources, uniform, best control of layer thickness	Slow, sophisticated, and expensive, very complicated system	Ultra-high vacuum, substrate temperature, deposition rate, process control unit
4.	Close spaced sublimation	Low vacuum at moderate temperature, simple deposition apparatus, less use of material	Difficult to monitor and control the thickness, costly	Vacuum pressure, substrate to source distance, substrate and source temperature
5.	Metal organic chemical vapor deposition	Highly flexible, uniform deposition	Highly toxic, very expensive source material	Deposition temperature, flow of reaction rate, vaporization rate
6.	Electrodeposition	Simple and fast process, very good adherence	Presence of impurities from solvent, thickness limitation	Current density, pH value, deposition time, bath temperature
7.	Screen printing	Easy process, low expenditure, large area of deposition	Low production rate, poor ink mileage, excessive drying time needed	The viscosity of the paste, the mesh number of screens, snap-off distance between the screen and substrate, pressure
8.	Sol-gel	Simplest, homogeneity, low cost, reliability, reproducibility	Long period of deposition, difficult to attach thick layer on substrate	Concentration of reactants, catalytic agents, precursors, morphology and transparency of gel,
9.	Spin coating	Easy to handle, cheap, high uniformity	Lack of material efficiency, coating material waste	Concentration of precursor material, speed of spin coater, deposition rate, temperature
10.	Spray pyrolysis	Low cost, easy set-up, applicable to large area,	Presence of impurities, less efficient, low quality of material deposition	Substrate temperature, spray rate, time, concentration of precursor material, pressure, carrier flow rate, nozzle to substrate distance,
11.	Successive ionic layer adsorption and reaction	Energy saving, low deposition rate	High working pressure needed, requirement of sophisticated environment	Temperature of solutions, nature of substrate, pH, concentration of solutions, dipping and rinsing time
12.	Chemical bath deposition	Low cost, easy set-up, stable, uniform, and hard film deposition	Wastage of solution, clean substrate is required	Temperature of solution, stirring time, concentration of precursor material, nature of substrate

nature of substrate [58, 62]. The quality of CdS thin film depends on the controlled precipitation of cadmium ions as well as sulfide ions. Complexing agents and/or catalysts, the liberation of hydroxyl ions with water, can control the precipitation of ions. Mainly, the growth of CBD-CdS thin films divided into two mechanisms heterogeneous reaction (i.e., ion-by-ion deposition) and homogeneous reaction (i.e., cluster-by-cluster deposition). In the heterogeneous mechanism, the cadmium ions and sulfide ions first attach on the substrate and then involve in chemical reaction for the formation of CdS, whereas in the homogeneous mechanism the ions get reacted and form CdS inside the solution and after that adhere onto substrate. Ion-by-ion mechanism for CdS deposition has advantages on the formation of stable, dense, and well-adherent compound material than cluster-by-cluster mechanism.

In this research, CdS thin films were synthesized over soda lime glass substrate by the CBD method. Two different CBD processes for CdS thin film deposition with various concentrations of precursor material, time of deposition, bath temperature, and complexing agent or buffer material were applied. This study was performed in order to analyze growth process mechanism, and optimize the material as buffer layer in thin film solar cells. The structural, morphological, optical, and electrical properties of CdS thin film synthesized by the CBD process with several growth methods were discussed. A systematic investigation on the effect of deposition temperature and time on the physical properties of CdS thin films by the CBD process was also reported.

## 2 Experimental

### 2.1 Materials details

Precursor materials used for the deposition process such as soda lime glass substrates (SLG, corning No 2947,  $75 \times 25 \times 1 \text{ mm}^3$ ), Extran solution, sodium hydroxide pellets (NaOH, 98.0%), hydrochloric acid (HCl, 37.0%), methanol, cadmium acetate dihydrate ( $\text{C}_4\text{H}_6\text{CdO}_4 \cdot 2\text{H}_2\text{O}$ , 98.0%), thiourea ( $\text{CH}_4\text{N}_2\text{S}$ , 99.0%), ammonium hydroxide solution ( $\text{NH}_4\text{OH}$ , 28.0–30.0%), and ammonium acetate were purchased from Sigma-Aldrich (chemicals company). Nitrogen ( $\text{N}_2$ ) gas cylinder was bought from INFRA group, Mexico.

### 2.2 Substrate cleaning

Thin-film materials are grown over soda lime glass substrates. The deposited films should stick effectively on the substrate for better growth of the CdS film. For this, the substrates must be cleaned properly. SLG substrates were, first, thoroughly cleaned ultrasonically with de-ionized water and then in the Extran solution. Subsequently, substrates were washed in

NaOH aqueous solution (2.5M) for 60 min, followed by HCl (0.1M) solution for 5 min, and finally cleaned with methanol (98%, pure) for 10 min. After cleaning in each solution, the substrates were washed by de-ionized (DI) water repeatedly. At last, cleaned substrates were dried by  $\text{N}_2$  gas flux and directly put in the film deposition process or save them in vacuum for later deposition.

## 2.3 Film deposition

### 2.3.1 Process one

CdS thin films were fabricated by CBD technique using cadmium acetate dihydrate aqueous solution (0.01 M) as a cadmium source, thiourea aqueous solution (0.29 M) as a sulfur source, and ammonium hydroxide aqueous solution (2.4 M). The ammonium hydroxide aqueous solution was used as a complexing agent as well as responsible for adjusting the pH of the final solution. The bath temperature was varied from 60 to 80 °C with varying deposition duration from 7 to 16 min. The order of the precursors was fixed by pouring cadmium source first, then thiourea source followed by ammonia source. Then the previously cleaned SLG substrates were vertically immersed into the solution as shown in the schematic diagram (Fig. 1). The precursor solution was stirred slowly during the solution preparation process. The samples were then rinsed with de-ionized water and dried by nitrogen gas at room temperature. Due to the quality of the films applicable for the CIGSe solar cell buffer layer, we limit our study to the samples deposited at 70 °C for different aging times.

From the cadmium side, the main chemical reactions involved in the formation of CdS films or colloids are as follows [37]:

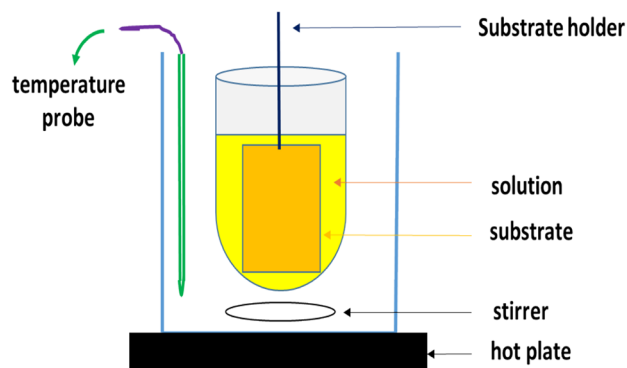
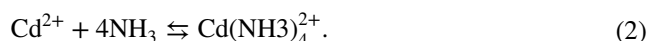
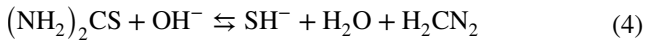
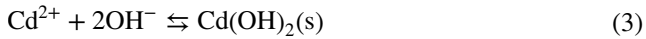


Fig. 1 Schematic diagram of chemical bath deposition

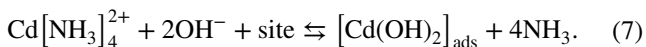
Here,  $\text{Cd}^{2+}$  is predominantly used up in Eq. 2 to form cadmium tetra-ammine complex ions ( $\text{Cd}(\text{NH}_3)_4^{2+}$ ), especially if  $\text{NH}_3$  concentration is sufficiently high. These ensure that the ionic product of  $[\text{Cd}^{2+}]$  and  $[\text{OH}^-]$  is less than the solubility product of  $\text{Cd}(\text{OH})_2$  and prevent the equilibrium reaction.



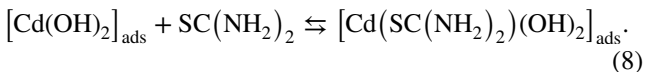
If the ionic product of  $[\text{Cd}^{2+}]$  and  $[\text{S}^{2-}]$  is greater than the solubility product of  $\text{CdS}$ , then Eq. 6 takes place.

Mechanism of  $\text{CdS}$  film growth on substrate can be explained explicitly as follows [63–65]:

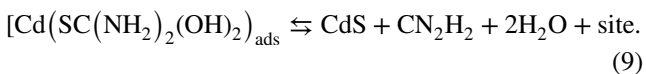
(a) Reversible adsorption of cadmium hydroxide species:



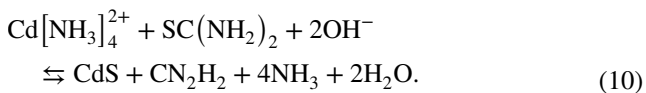
(b) Formation of surface complex with thiourea:



(c) Formation of  $\text{CdS}$  with site generation:



The overall reaction is given below:



### 2.3.2 Process two

The chemical bath deposition process was carried out for the deposition of cadmium sulfide thin film using various precursor materials such as cadmium acetate (cadmium source), thiourea (sulfur source), ammonium hydroxide (complexing agent), and ammonium acetate (catalytic reagent). The CBD method is mainly based on the slow release of cadmium ions and sulfur ions inside the chemical bath and then condensation of  $\text{CdS}$  thin films on the substrate. First of all,  $\text{CdS}$  thin films were deposited at several proportions of ammonium hydroxide from 1:1 to 5:1 compared with cadmium acetate and thiourea. After that,  $\text{CdS}$  thin films were fabricated on different bath temperatures (70, 75, 80, and 85 °C) at a

constant time of 30 min and different timings (20, 30, 40, 50, and 60 min) at constant bath temperature of 80 °C. The substrates were mounted vertically with the help of Teflon holders inside the solution. Precursor solution was prepared by dissolving 0.033 M of cadmium acetate (as cation ( $\text{Cd}^{2+}$ ) source), 0.7 M of thiourea (as anion ( $\text{S}^{2-}$ ) source), 3 M of ammonium hydroxide, and 1 M of ammonium acetate on 200 mL of de-ionized water. The stirring action inside the bath helps to interact between substrate and reactants that is also significant for uniform deposition. When all the precursor solutions are mixed, the chemical reactions between cadmium ions and sulfur ions begin and the color of the solution changes into a yellow color that signifies the formation of  $\text{CdS}$  material. After the deposition, the substrates were taken out from the solution and then ultrasonically rinsed with de-ionized water for 2–3 min to remove loosely bonded  $\text{CdS}$  particles. Finally, the films were washed with running de-ionized water and dried with nitrogen gas to get rid of moisture. The rear side film of the substrate was removed with the help of the  $\text{HCl}$  solution in order to characterize the film.

The ammonia was used as a complexing agent which controls the free cadmium metal ion concentration and produces free cadmium ions ( $\text{Cd}^{2+}$ ) through dissociation reaction. Ammonium acetate was applied as a buffer solution to control the cadmium concentration as well as reaction rate. Ammonia and ammonium acetate combined with water liberate the hydroxyl ions ( $\text{OH}^-$ ) that reacts with cadmium acetate giving cadmium hydroxide and with thiourea providing free sulfur ions. The cadmium hydroxide in the presence of ammonium hydroxide produces cadmium tetramine complex ions and hydroxyl ions. The produced hydroxyl ions serve to maintain a constant pH value (= 10) of the bath. Finally, the complex ions mixed with sulfur ions form cadmium sulfide compound. The possible reactions that occur in this growth process are shown in equation from 11 to 19 and the schematic diagram of the experimental details of process two is shown in Fig. 2.

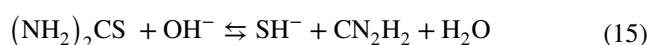
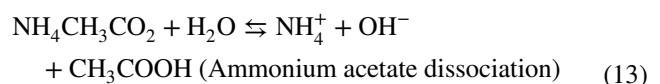
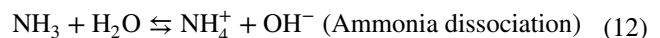
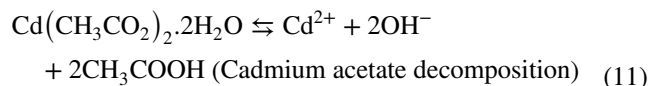
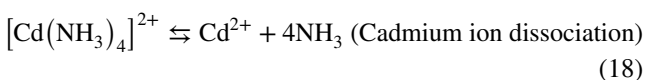
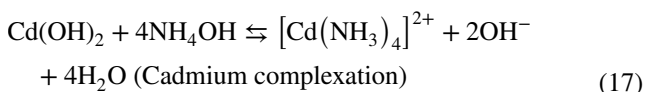
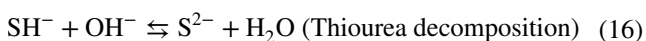
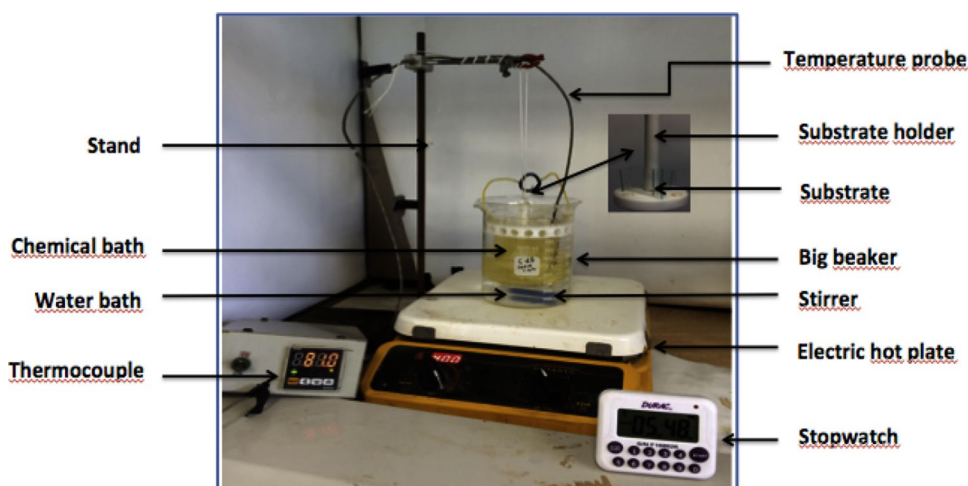




**Fig. 2** Experimental details of process two



## 2.4 Film characterization

Bruker's DektakXT stylus profiler estimated the thickness of the deposited CdS films. A necessary step for measuring the film thickness was done by dipping the film in a 10% v/v of HCl solution. The information about the crystallinity, crystallite size, and the phase assessment of the CdS films was carried out using X-ray diffraction (XRD) recorded on an X'Pert PRO diffractometer-PANalytical using Cu-K $\alpha$  ( $\lambda = 1.5406 \text{ \AA}$ ) radiation at grazing incidence of  $0.5^\circ$  in the  $2\theta$  ranging from  $20^\circ$  to  $80^\circ$ . The micro-Raman spectra of fabricated films were obtained by the HORIBA Jobin Yvan system with He-Ne laser (632 nm) at room temperature. The morphological studies were carried out using the TESCAN VEGA scanning electron microscope (SEM) on the surface of the deposited CdS thin films. Atomic force microscope (AFM) (NT-MDT, NTEGRA spectra) analysis was carried out in non-contact mode, to investigate the topographical information of the deposited films. Optical transmittance and reflectance of the films were measured in the wavelength range of 300–1100 nm by JascoV-670 spectrophotometer. The absorption coefficient ( $\alpha$ ) was calculated from the

transmittance data, and the Tauc plot was used to determine the band gap of the films. The photoluminescence spectra at room temperature of the synthesized CdS thin films were measured on a spectrofluorometer using a He-Ne laser as the excitation light source.

## 3 Result and discussion

### 3.1 Growth rate

#### 3.1.1 Process one

We have reported the variation of the deposition rate of CdS thin films as a function of the bath temperature for different deposition times. As seen in Fig. 3, the deposition rate is increasing with increasing bath temperature along with the deposition time indicating a significant dependence of the growth rate on temperature and time [66]. The growth rate increased while increasing the deposition time from 7 to 16 min in all the batches of bath temperature (60, 70, and 80 °C). The highest growth rate, equal to  $7.71 \text{ nm min}^{-1}$ , was reported with the film growth at 80 °C; however, at low temperature (60 °C) the deposition rate was around  $2.85 \text{ nm min}^{-1}$ . The film thickness is the most reported parameter rather than the deposition rate in the application of the buffer layer in solar cells. The increase in the deposition rate with the bath temperature was due to the kinetic enhancement of the involved reaction during the nucleation growth of the film [67]. The deposition rate obtained at 80 °C was 2–3 times greater than that obtained at 60 °C for the film deposited for 7 and 10 min. This influence was due to the activation of the chemical reaction between the species leading to the formation of CdS films from alkaline solutions. The activation energy of the film growth and the formation enthalpy

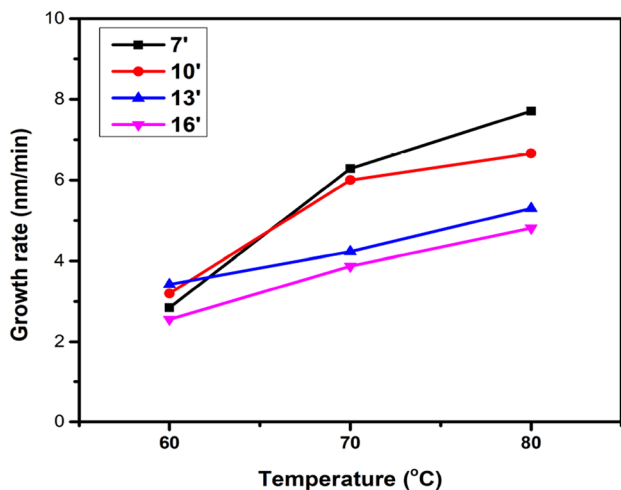


Fig. 3 Growth rate of CdS thin films deposited by CBD at different temperatures

of Cd<sup>2+</sup> could be responsible for varying the growth rate of the CdS thin film [68, 69]. The growth rate for lower temperatures was due to the domination of the ion-by-ion reaction mechanism. Higher temperature means the increment of free ions (Cd<sup>2+</sup> and S<sup>2-</sup>) concentration in the bath, which increases the growth rate and hence film thickness.

### 3.1.2 Process two

The nucleation and growth rate of films also depend on the nature of energy applied for the formation of the film. The physical properties of thin films such as the quantum size effect and color of the film rely on the thickness. Figure 4 displays the variation of the deposition rate of CdS thin films grown at different temperatures (constant time of 30 min) and at various times (constant bath temperature of 80 °C). The growth rate of the film increases with a rise in the bath temperature as well as the time of deposition that might be due to kinetic enhancement of reactions with increase in the mobility of the ions during deposition. The higher amount of cadmium and sulfide ion concentrations inside the chemical bath are formed as we increase the temperature and time of deposition. It is observed that the growth rate of the film enhances at higher deposition temperatures and times. As seen from the data, the minimum deposition rate was found around 1 nm/min for a lower value of deposition temperatures and times and more than 5 nm/min growth rate at higher deposition temperatures and times.

### 3.2 X-ray diffraction (XRD) analysis

The average crystallite size (D) was calculated by using a Scherrer’s formula [64]:

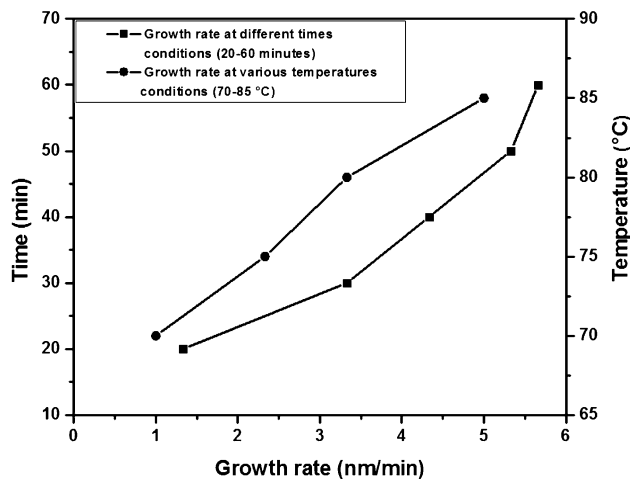


Fig. 4 Graphical representation of growth rate of CdS thin films deposited at different temperature and time conditions

$$D = \frac{K\lambda}{\beta \cos\theta}, \tag{20}$$

where *K* is the Scherrer constant or shape factor (*K*=0.9, assuming spherical crystallites),  $\lambda$  is the wavelength of incident X-ray ( $\lambda = 1.5406 \text{ \AA}$ ),  $\beta$  is the full width at half maximum (FWHM in radians) of the peak corrected for instrumental broadening, and  $\theta$  is the Bragg’s diffraction angle.

The inter-planar spacing (*d*), lattice parameters (*a* and *c*), strain ( $\epsilon$ ), dislocation density ( $\delta$ ), and crystallite number per unit surface (*N*) for a dominant peak were calculated from the following equations [68–73]:

$$2d \sin \theta = n\lambda \tag{21}$$

$$\frac{1}{d^2} = \frac{4}{3} \left( \frac{h^2 + hk + k^2}{a^2} \right) + \frac{l^2}{c^2} \tag{22}$$

$$\epsilon = \frac{\beta \cos\theta}{4} \tag{23}$$

$$\delta = \frac{1}{D^2} \tag{24}$$

$$N = \frac{t}{D^3}, \tag{25}$$

where *h*, *k*, *l* are the Miller indices and *t* is the thickness of CdS thin films.

#### 3.2.1 Process one

The properties of the CdS thin film have been investigated by X-ray diffraction (XRD) technique, as shown in Fig. 5,

synthesized by CBD method to analyze the crystalline structure for different deposition durations (7, 10, 13, and 16 min) at a bath temperature of 70 °C on a glass substrate. XRD pattern provided the information about the crystalline phase of the CdS thin films as well as crystallite size. All the deposited CdS films were polycrystalline in nature with a preferential orientation plane (002) perpendicular to the substrate corresponding to an international center for diffraction data (ICDD) No. 01-083-5246 having a hexagonal (wurtzite) crystalline structure [70, 71]. We can see from the diffraction pattern that the peak intensity was increased as the deposition time increases, and this was due to the growth of the material involved in the deposition mechanism which corresponds to the thickness of the CdS thin film. For all the samples, we have observed that an intense peak appeared at two-theta ( $2\theta$ ) value approximately 26.5°, which corresponds to the CdS hexagonal plane (002), or cubic plane (111), but the peak corresponding to the plane (110) at  $2\theta$  value around 44.4° and the plane (112) at around 52.2° indicated that the phase belongs to hexagonal or at least a mixture of hexagonal or cubic [72]. The noise and hump around the peaks do not allow us to distinguish the crystallographic structure of the CdS films because of the penetration depth while taking XRD pattern even from grazing incidence due to ultrathin applicable for buffer layer in CIGSe-based solar cell. The value of crystallite size was decreased with increasing the deposition duration. With the increase of aging time, there was an increase in intensity and sharpness of the predominant peak, which is caused by the improvement on the crystallinity of the CdS thin films. The crystallite size was varied from 27.57 to 15.46 nm with increasing deposition duration from 7 to 16 min at 70 °C of bath temperature

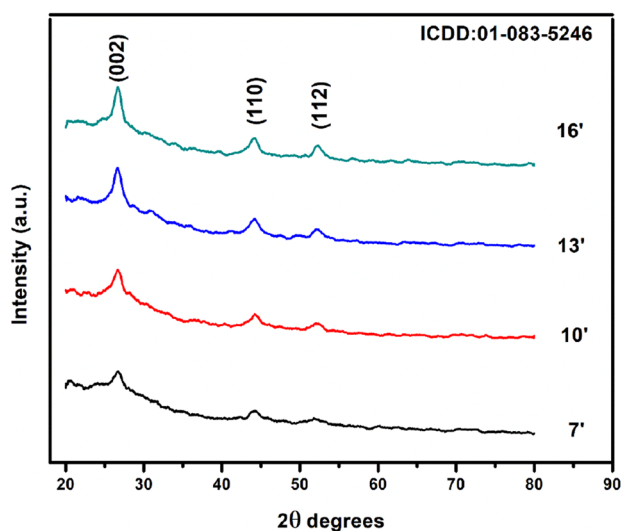


**Fig. 5** XRD pattern of CdS thin film deposited by CBD at 70 °C for different deposition times

estimated from the most intense peak which corresponds to the plane (002) as shown in Table 2. The observed decrease in the crystallite size with an increase in deposition duration is due to the complete deposition process occurring through three regimes namely nucleation, coalescence, and subsequent vertical growth of CdS thin films.

### 3.2.2 Process two

The preferred orientation CdS thin films is influenced by the source compound, nucleation process, and growth parameters of various deposition methods. In most of the research papers, XRD studies of physical vapor deposition revealed that deposited CdS thin films have dominant hexagonal structure and solution growth deposition has dominant hexagonal or dominant cubic or mixed (cubic + hexagonal) crystal structure [41–58]. The crystallinity of CdS film was different for different fabrication processes, which may be due to the different nucleation and growth rate for various deposition methods [74]. For thin-film solar cell, a buffer layer with hexagonal structure is preferred over the cubic one due to its stable nature, higher optical band gap, as well as mismatching lattice parameters [75]. XRD analysis was performed in the range of angle two-theta lying between 10 to 70° in order to find the crystallite size and also to study the structural properties of CdS thin films (see in Fig. 6). In both cases, XRD results display the major reflection of (002) located at  $2\theta$  value of around 26.7° that correspond to the hexagonal crystal structure of CdS. The presence of minor reflections like (100), (101), (110), 103, and (112) are compatible with the hexagonal structure of CdS thin films. The strong and sharp diffraction peaks of (002) increases with increasing deposition time and temperature; is the consequence of increase in thickness due to decomposition of reactants and production of ions that lead to improve the crystallization of films. The hexagonal system of lattice planes of CdS thin films was verified with the joint committee powder diffraction system (JCPDS Card Number: 01-074-9664 with lattice constants,  $a = 4.1002 \text{ \AA}$ ,  $c = 6.6568 \text{ \AA}$ , and  $c/a = 1.62$  and inter-planer spacing ( $d$ ) = 3.3284 Å) which is well matched with the calculated value. Table 3 shows X-ray diffraction data of  $2\theta$ , full width half

**Table 2** Calculated structural parameters of CdS thin films deposited by CBD at 70 °C

Deposition time (min)	D (nm)	$\delta (\times 10^{-3} \text{ lines/nm}^{-2})$	N ( $1/\text{nm}^2$ )	$\epsilon (10^{-3})$	c/a
7	27.570	1.315	2.099	1.257	1.617
10	20.660	2.342	6.804	1.677	1.638
13	17.550	3.246	10.173	1.974	1.647
16	15.460	4.183	16.508	2.241	1.651



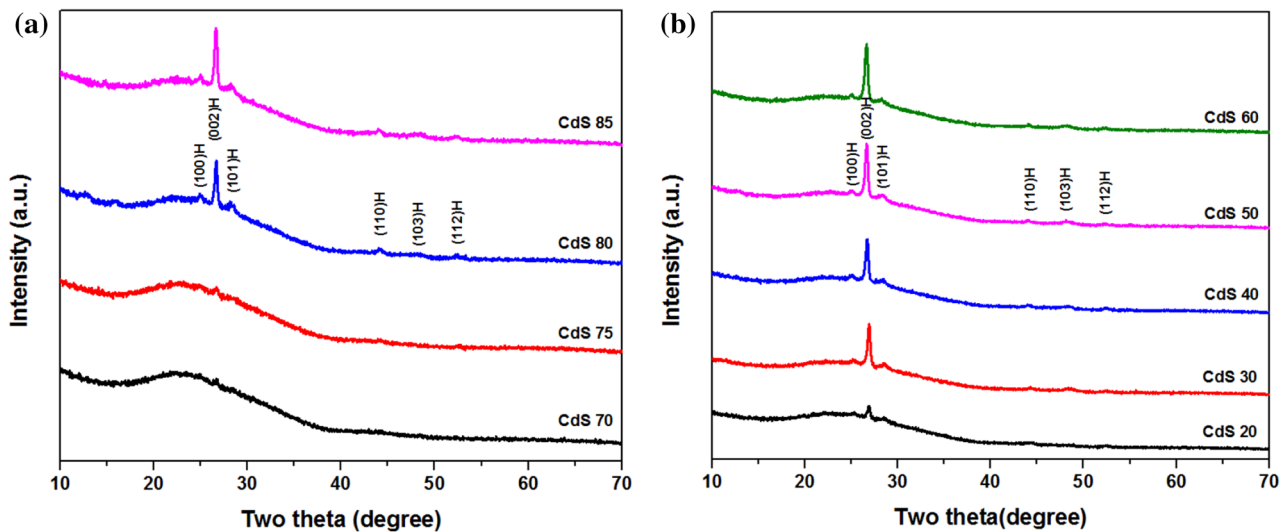


**Fig. 6** XRD patterns of CdS thin films at different deposition **a** temperatures and **b** times

maximum (FWHM), crystallite size, strain, dislocation density, crystallite number per unit surface, inter-planer spacing, and lattice constants for various deposition times and temperatures of CdS thin films. It is found that the intensity of the peaks increases and the width of peak decreases due to improved crystallinity with an increase in substrate temperature and deposition time (except at 60 min). And also, it is seen that  $2\theta$ , FWHM, strain, dislocation density value decreases in higher deposition temperatures as well as times. The decrease in strain due to the growth of film thickness demonstrates the reduction in the cohesive force between films and a substrate material that represents the decrease in lattice imperfection and increase in the crystallite size.

### 3.3 Raman spectroscopy

#### 3.3.1 Process one

Raman spectroscopy is based on inelastic scattering of monochromatic light upon interaction with the sample. The shift in the frequency-emitted photons is a signature and explains the different frequency modes like vibrational, rotational, and other low frequency transitions in the molecules. Raman spectroscopy is a powerful technique for identifying the lattice defect, concentration of dopant, and the crystal orientation of the materials. However, it cannot be used to distinguish the two structure of CdS thin film because the frequency of the hexagonal modes nearly matches to those of cubic modes. Figure 7 shows the Raman spectra of chemically deposited CdS films in which two peaks, corresponding

**Table 3** Calculated structural parameters of CdS thin film deposited at different times and temperatures

Parameters Sample	$2\theta$ (degree)	FWHM ( $\times 10^{-3}$ Rad)	Crystallite Size (D) (nm)	Strain ( $\epsilon$ ) ( $\times 10^{-3}$ Rad)	Dislocation density ( $\delta$ ) ( $\times 10^{-3}$ lines/nm <sup>2</sup> )	$N = t/(D^3)$ ( $\times 10^{-3}$ nm <sup>-2</sup> )	Inter-planer spacing (d) (Å)	Lattice constants	
								c (Å)	a (Å)
CdS 70 °C 30 min	26.70	6.8	28.78	1.20	1.21	1.26	3.336	6.672	4.44
CdS 75 °C 30 min	26.69	6.6	29.51	1.17	1.15	2.73	3.337	6.675	4.45
CdS 80 °C 30 min	26.66	5.4	35.54	0.97	0.79	2.22	3.341	6.682	4.45
CdS 85 °C 30 min	26.64	4.8	39.61	0.87	0.64	2.42	3.343	6.687	4.45
CdS 80 °C 20 min	26.92	5.7	38.67	0.89	0.67	0.87	3.310	6.620	4.43
CdS 80 °C 30 min	26.87	5.2	41.44	0.84	0.58	1.40	3.316	6.633	4.43
CdS 80 °C 40 min	26.70	4.9	39.95	0.87	0.63	2.05	3.336	6.672	4.25
CdS 80 °C 50 min	26.64	4.7	40.45	0.85	0.61	2.41	3.343	6.687	4.46
CdS 80 °C 60 min	26.62	5.4	34.88	0.99	0.82	3.99	3.346	6.692	4.46

to the first and second longitudinal optical phonon modes, were identified. The 1LO and 2LO peaks were strong and weak correspond to the fundamental and overtone modes, respectively [76]. The 1LO peak was shifted from 304 to 301  $\text{cm}^{-1}$  while increasing the deposition time from 7 to 16 min. Also, the intensity and sharpness of fundamental mode (1LO) were increased with the increase of deposition time indicating the enhancement in the crystal structure which was in close agreement to the XRD results. The average FWHM was also decreased from 19  $\text{cm}^{-1}$  (at 7 min) to 13  $\text{cm}^{-1}$  (at 16 min) resulting in better crystallinity for more deposition time. Besides the fundamental (1LO) mode, overtone (2LO) modes were located at 602  $\text{cm}^{-1}$  in all the

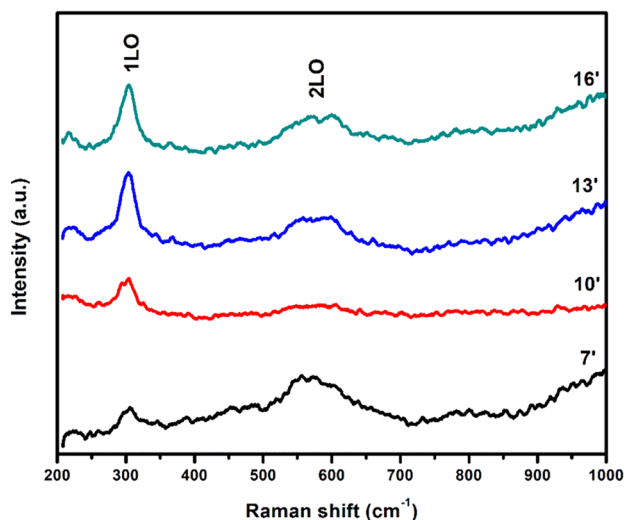
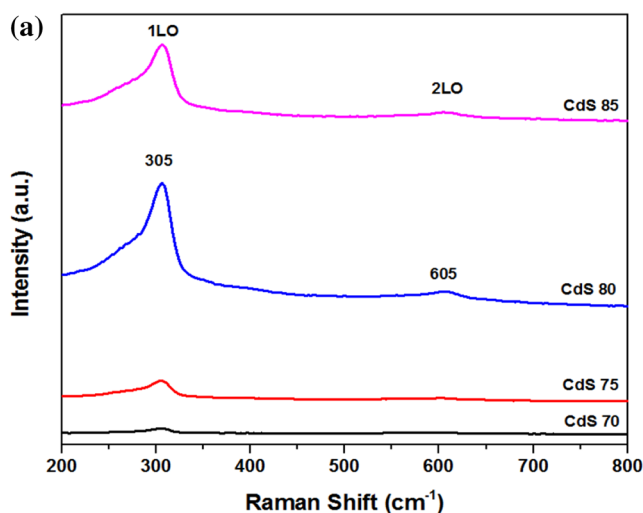


**Fig. 7** Raman spectra of CdS thin films deposited by CBD at 70 °C for different deposition times



deposited CdS thin films, which is almost closed to the literature value of bulk CdS (605  $\text{cm}^{-1}$ ) [77–79]. The position of the 1LO and 2LO modes in the prepared CdS thin films was shifted by a little in accordance to bulk CdS due to the phonon confinement effect.

### 3.3.2 Process two

In both deposition times and temperatures (Fig. 8), the first-order scattering of the longitudinal optical (1LO) phonon was observed at 305  $\text{cm}^{-1}$  and the second-order scattering of longitudinal optical (2LO) phonon found at 605  $\text{cm}^{-1}$ . 1LO and 2LO peaks shifted to lower values in vacuum-based methods might be due to size effect or surface phonon mode effect and mechanical stress in the interface. The hexagonal wurtzite structure of CdS thin films corresponds to these two longitudinal optical phonons [80, 81]. The variations in Raman shift and peak intensity depend mainly on the composition of elements, variation in crystallite size, as well as impurity present (i.e., oxygen incorporation into the lattice) inside the film [82]. Here, the intensity of the 1LO peak of CdS thin films increases at a higher value of deposition temperatures and times that signify the enhancement of crystal structure of films. The similar results of Raman spectra can also be found in various scientific researches [83, 84].

## 3.4 Morphological analysis

### 3.4.1 Process one

The film exhibited hexagonal crystal structure invariably grow with columnar structure along the *c*-axis perpendicular to the substrate, introducing fewer grain boundaries parallel

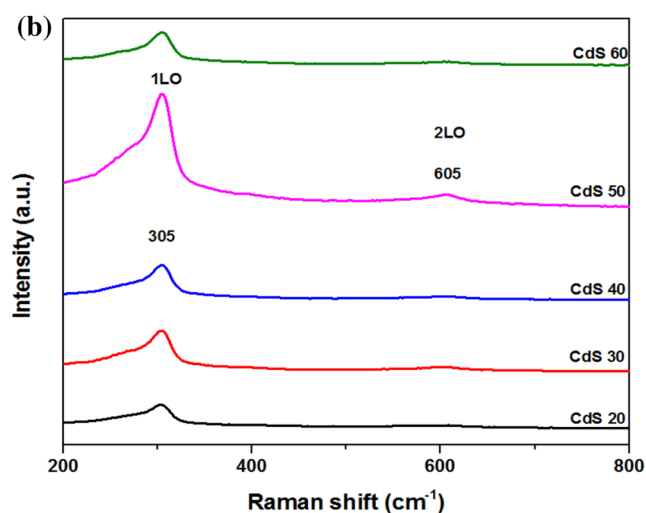


**Fig. 8** Raman spectra of CdS thin films deposited at different deposition **a** temperature and **b** time conditions

to the junction which can restrict the flow of the photogenerated excess carriers to the grid [85]. Figure 9 illustrates the SEM micrographs of the surfaces of the CdS films deposited at 70 °C for different deposition durations (7, 10, 13, and 16 min). These micrographs exhibit that the deposition duration affects the surface morphology of the CdS thin film. Increasing the deposition duration resulted in an increase in grain size but some pinholes can be seen for the CdS films deposited for 13 and 16 min. The film deposited for 7 min had an average grain size of 60 nm, while the film deposited for 13 and 16 min had a larger grain size (> 90 nm) with voids indicating low packing density of the film. The surface of the CdS film deposited for 10 min has compact and smooth grains, showing granular structure with well-defined grain boundaries with very less pinholes.

The chemical composition of CdS thin films was analyzed by energy dispersive X-ray spectroscopy (EDS). The EDS spectrum of the CdS thin film deposited at 70 °C for 10 min is shown in Fig. 9a. The pattern showed the peaks besides Cd and S due to the impurities from glass substrate and gold (Au) during sample coating. The chemical composition of the CdS thin films deposited at 70 °C for the different durations can be seen in Table 4 and the Cd/S ratio for all the samples was greater than 1.

### 3.4.2 Process two

The SEM micrographs of CdS thin films prepared with various deposition temperatures and times are shown in Fig. 10 and confirm that the microstructure of thin films changes with different conditions. It is seen from the images that the particles have distinct features composed of sphere-like structure with grain size distribution in a range of 10–20 nm. The sample deposited at low temperature shows the non-uniform distribution of agglomerated particles with large number pinholes in it. Therefore, the films prepared at low temperatures and time showed a larger number of grain boundaries density, lower crystallinity, and higher resistivity. The continuous and dense, homogeneous film without

**Table 4** EDS compositional details of CdS thin film

Dep. Time (min)	Cadmium (Cd) %	Sulfur (S) %	Cd/S ratio
7	50.67	49.33	1.02
10	51.83	48.17	1.07
13	52.01	47.99	1.08
16	53.59	46.41	1.15

cracks, smooth surface, fine spherical structure without any voids can be observed at higher deposition temperature and time due to slow deposition rate and ion-by-ion mechanism of film formation. The formation of spherical granules on the scanned image might be due to the spheroid structure of sulfur ions. The CdS thin films grown at a slow deposition rate led to the formation of a uniform film, fewer pinholes, and good adhesion to the substrate than deposition at a high rate [86].

EDS analysis was performed on CBD-CdS thin films where the average atomic compositions of the films were taken by mean of the data collected from random points. From Table 5, the cadmium concentration decreases from 67–50% and sulfur concentration increases from 33 to 50% with an increase in both temperature and time of deposition. As seen, the sample with higher amounts of sulfur shows eminent crystallinity, improved morphology, as well as better conductivity due to interstitial sulfur. The presence of cadmium and sulfur atoms in the film verified by the EDS spectrum (see in Fig. 11a) and homogeneous distribution of CdS molecule were seen in EDS mapping shown in Fig. 11b.

## 3.5 Topographical analysis

### 3.5.1 Process one

Atomic force microscopy (AFM) is the most versatile and powerful technique for the analysis of samples in the nano-scale level. This technique provides various types of

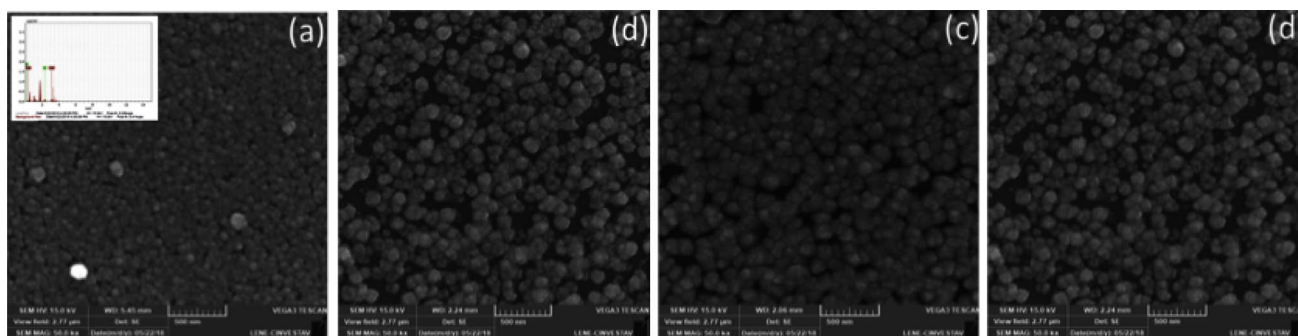


**Fig. 9** SEM images of CdS thin films at 70 °C for different deposition times **a** 7 min, **b** 10 min, **c** 13 min, and **d** 16 min

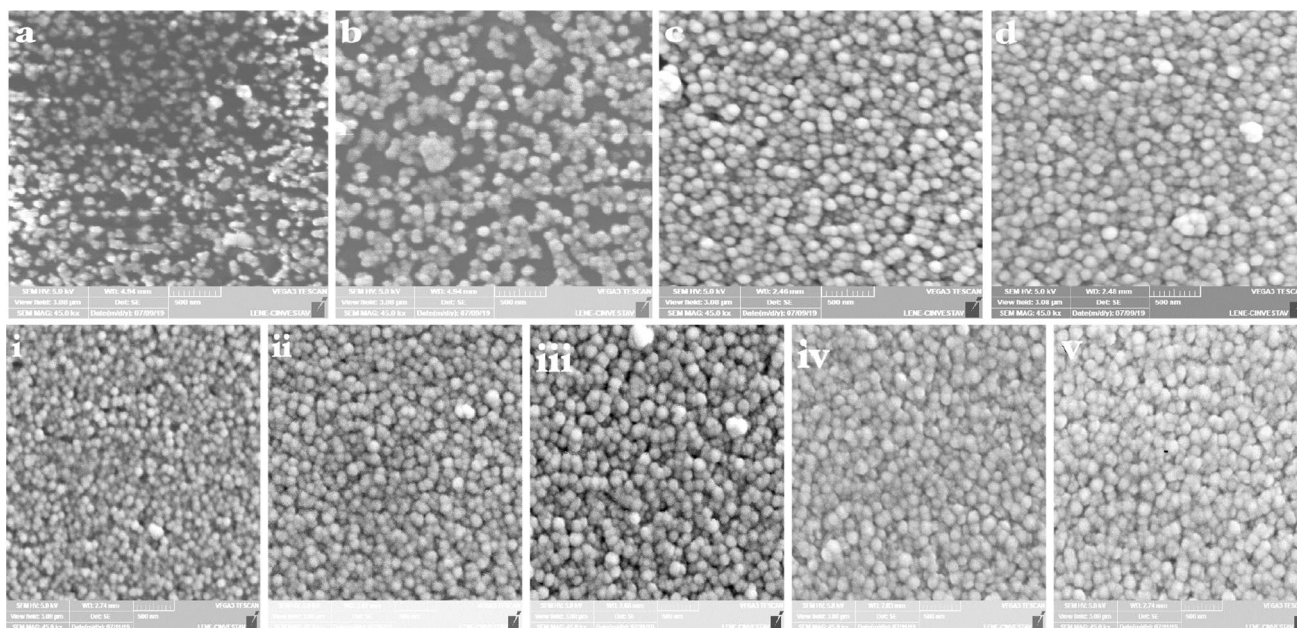


Fig. 10 SEM images of CdS thin films deposited at various deposition (a–d) temperatures and (i–v) times

Table 5 Compositional analysis of CdS thin films by process two

Sample (temperatures, times)	Cadmium (%)	Sulfur (%)	Cd/S
CdS 70 °C 30 min	67	33	2.03
CdS 75 °C 30 min	57	43	1.33
CdS 80 °C 30 min	55	45	1.20
CdS 85 °C 30 min	52	48	1.08
CdS 80 °C 20 min	55	45	1.20
CdS 80 °C 30 min	54	46	1.17
CdS 80 °C 40 min	53	47	1.13
CdS 80 °C 50 min	52	48	1.08
CdS 80 °C 60 min	52	48	1.08

surface measurements like grain size, RMS roughness, average roughness, peak-to-peak height, skewness, and kurtosis. Two-dimensional AFM images of CdS thin films, with scanning an area of  $2 \times 2 \mu\text{m}^2$  the surface of the films, are presented in Fig. 12. The surface shows distinct grain distribution with compact granular topography. The grain size was varied from 58 to 120 nm depending upon whether the deposition time and the average roughness of the deposited CdS thin films were around 3–9 nm (see in Table 6). The higher value of roughness was due to the presence of hill height for the sample deposited for 13 min because of a large number of nucleation and larger grain growth [87].

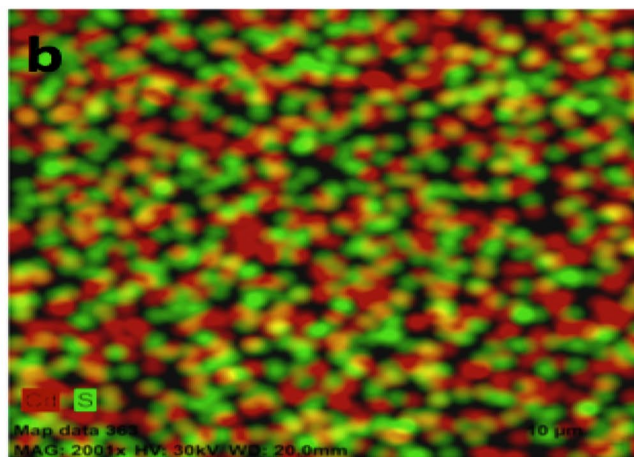
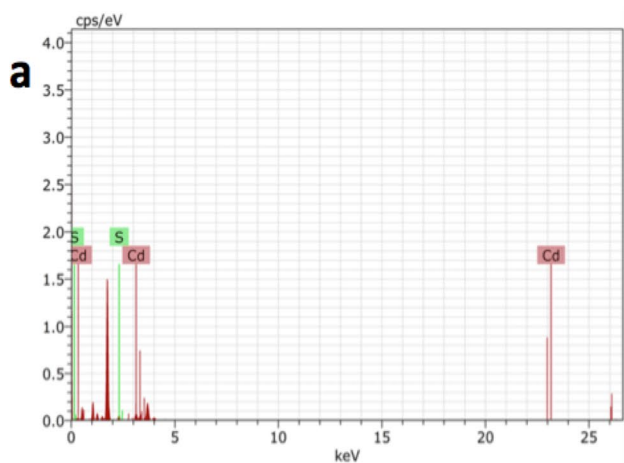
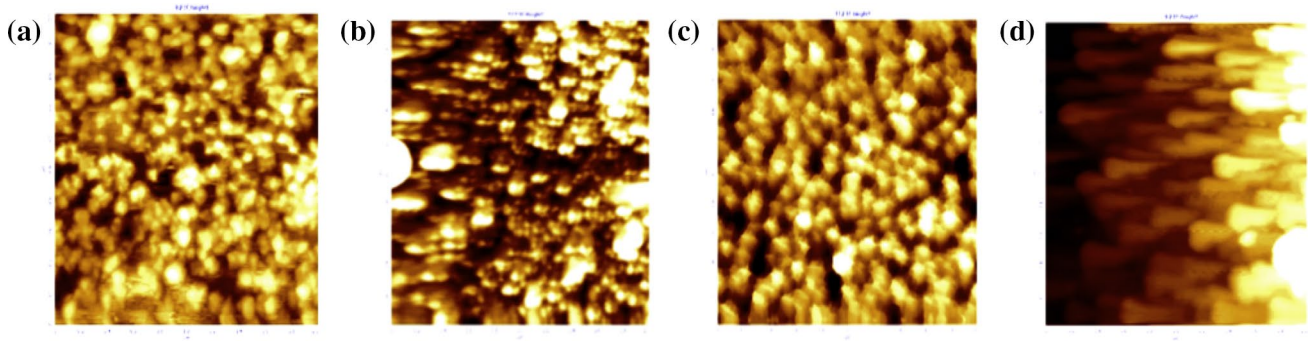


Fig. 11 Plot of a EDS spectrum and b EDS Mapping of CdS thin film deposited at 80 °C for 30 min





**Fig. 12** 2D AFM images ( $2 \times 2 \mu\text{m}$ ) of CdS thin films at  $70^\circ\text{C}$  for different deposition times **a** 7 min, **b** 10 min, **c** 13 min, and **d** 16 min

**Table 6** Calculated parameters—root mean square roughness (RMS), average roughness (Rav), skewness ( $S_{sk}$ ), kurtosis ( $S_{ka}$ ), and grain size of CdS thin film deposited at  $70^\circ\text{C}$  for different deposition durations

Parameters	7 min	10 min	13 min	16 min
RMS roughness (nm)	4.82	9.14	11.86	12.89
Rav (nm)	3.83	6.62	5.87	9.29
Skewness ( $S_{sk}$ )	0.45	0.74	1.48	1.34
Kurtosis ( $S_{ka}$ )	3.34	5.07	5.69	6.92
Grain size (nm)	47	57	69	83

The parameters such as skewness ( $S_{sk}$ ) and kurtosis ( $S_{ka}$ ) give the measurement of the asymmetry and the sharpness, respectively. Specifically, the profile symmetry about the mean line is measured by skewness ( $S_{sk}$ ). Hence, the value of skewness ( $S_{sk}$ ) can either be zero, positive, or negative. The skewness factor becomes zero if the height distribution is symmetrical. For an asymmetrical height distribution, the surface has more peaks than valleys leading to a positive value of skewness. If the surface of the film is more planar, then the value of skewness turns out to be negative. Another parameter kurtosis ( $S_{ka}$ ) measures the peakedness of the distribution with a reference value of 3. If the kurtosis value is equal to 3 signifies the mesokurtic (Gaussian amplitude distribution), and platykurtic if less than 3 which indicates that the surface is flat. The kurtosis factor greater than 3 shows the surface has more peaks than valleys.

### 3.5.2 Process two

Topographical analysis on the CdS thin films has been done by using atomic force microscopy (AFM) where the image can be studied through the convolution of the tip of the cantilever and the samples. The non-contact AFM operation mode was used to analyze the surface of the samples. It is observed, from Fig. 13, that the particles are uniformly distributed on the surface of the film and also the surfaces are composed of nano-sized grains with an approximate

size of 80–110 nm. In both conditions, CdS thin films were composed of a spherical shaped particulate, very well-connected grains without crack that presents an inhomogeneous compact surface. The grains were grouped together to form large clusters like cauliflower with an average size of around 200–400 nm. The values of average grain size, average roughness, skewness, and kurtosis are shown in Table 7. The surface roughness of the films lies in the range of 6–15 nm that signifies the formation of smooth as well as well-connected grains on the films. The value of skewness was positive as well as small value, near to zero, that represents the surface has more peaks than valleys and the height distribution is near to symmetrical. This information can also be verified by the data of kurtosis, which was greater than the value of 3.

### 3.6 Optical properties analysis

UV–Vis spectrometry is utilized to observe the optical properties such as transmission, reflection, and optical band gap of films that provide useful information to analyze some features concerning the band structure of materials. During the scanning process of transmission spectra, the soda lime glass substrate was put in one side of the light beam direction and the CdS film-deposited soda lime glass substrate was placed in the other direction of spectrometry.

The crucial parameter for photovoltaic cells is the optical band gap energy of material that helps to study the fundamental absorption, generation of electron–hole pairs, of light energy. With the results of transmittance and thickness of the material, the optical absorption coefficient ( $\alpha$ ) was calculated by using the following relation [88–91]:

$$\alpha = \frac{1}{t} \ln \left[ \frac{1}{T} \right], \quad (26)$$

where  $t$  is the thickness of the film and  $T$  is the transmittance.

We can determine the band gap energy of material by using following Tauc relationship:



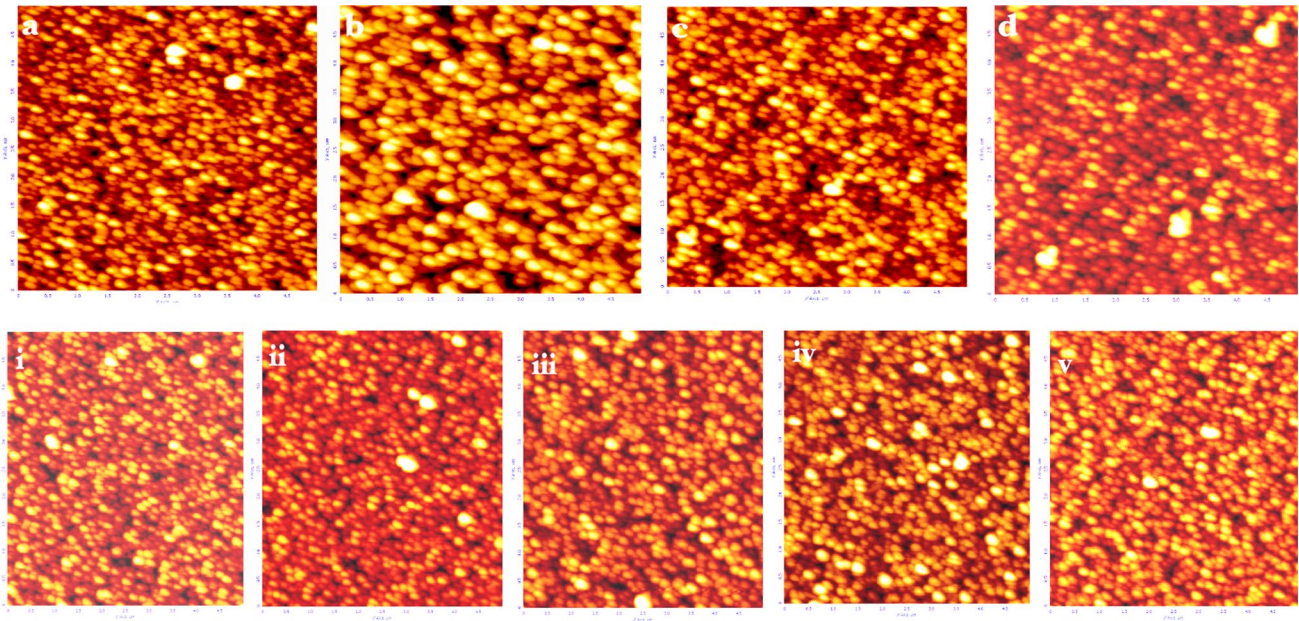


**Fig. 13** 2D AFM images ( $2 \times 2 \mu\text{m}$ ) of CdS films at different deposition **a–d** temperatures and **i–v** times

**Table 7** Parameters such as average grain size, average roughness, RMS roughness, skewness, kurtosis calculated from AFM

Parameters Sample	Average grain size (nm)	Average Roughness (nm)	RMS Roughness (nm)	Skewness ( $S_{sk}$ )	Kurtosis ( $S_{ka}$ )
CdS 70 °C 30 min	80	8	9.86	0.084	3.31
CdS 75 °C 30 min	111	14	10.39	0.031	3.49
CdS 80 °C 30 min	95	7.48	9.32	0.308	2.95
CdS 85 °C 30 min	95	7.41	9.48	0.407	3.95
CdS 80 °C 20 min	89	6.9	8.7	0.022	3.16
CdS 80 °C 30 min	89	6.4	8.3	0.372	4.31
CdS 80 °C 40 min	95	8.7	11.05	0.111	3.46
CdS 80 °C 50 min	90	7.17	9.14	0.147	3.30
CdS 80 °C 60 min	88	6.4	8.04	0.036	3.19

$$(\propto h\nu) = A (h\nu - E_g)^n, \quad (27)$$

where  $h\nu$  is the photon energy,  $A$  is a constant, and  $E_g$  is the optical band gap of the semiconductor materials.

We know  $n=2$  for indirect band gap semiconductor like Silicon,

and  $n = 1/2$  for direct band gap semiconductor material such as CdS.

Hence, the Tauc relation for the estimation of band gap of CdS thin films is

$$(\propto h\nu)^2 = A (h\nu - E_g). \quad (28)$$

### 3.6.1 Process one

Optical properties study of the thin films of CdS plays an important role in understanding the performance of the complete solar cell. The optical properties of thin film can affect the characteristics incident light spectrum. Our optical investigation and analysis of CdS thin film rely on measurements of transmittance, reflectance, and absorbance in the spectral range 300–1100 nm as shown in Fig. 14a–c. These optical studies were applicable to determine optical energy gap ( $E_g$ ), optical absorption ( $\alpha$ ), and optical penetration depth ( $\delta$ ). Transmission and reflection measurements were performed at room temperature to study the optical properties of the CdS thin film obtained at 70 °C of bath temperature for different deposition times. Due to the ultrathin nature of

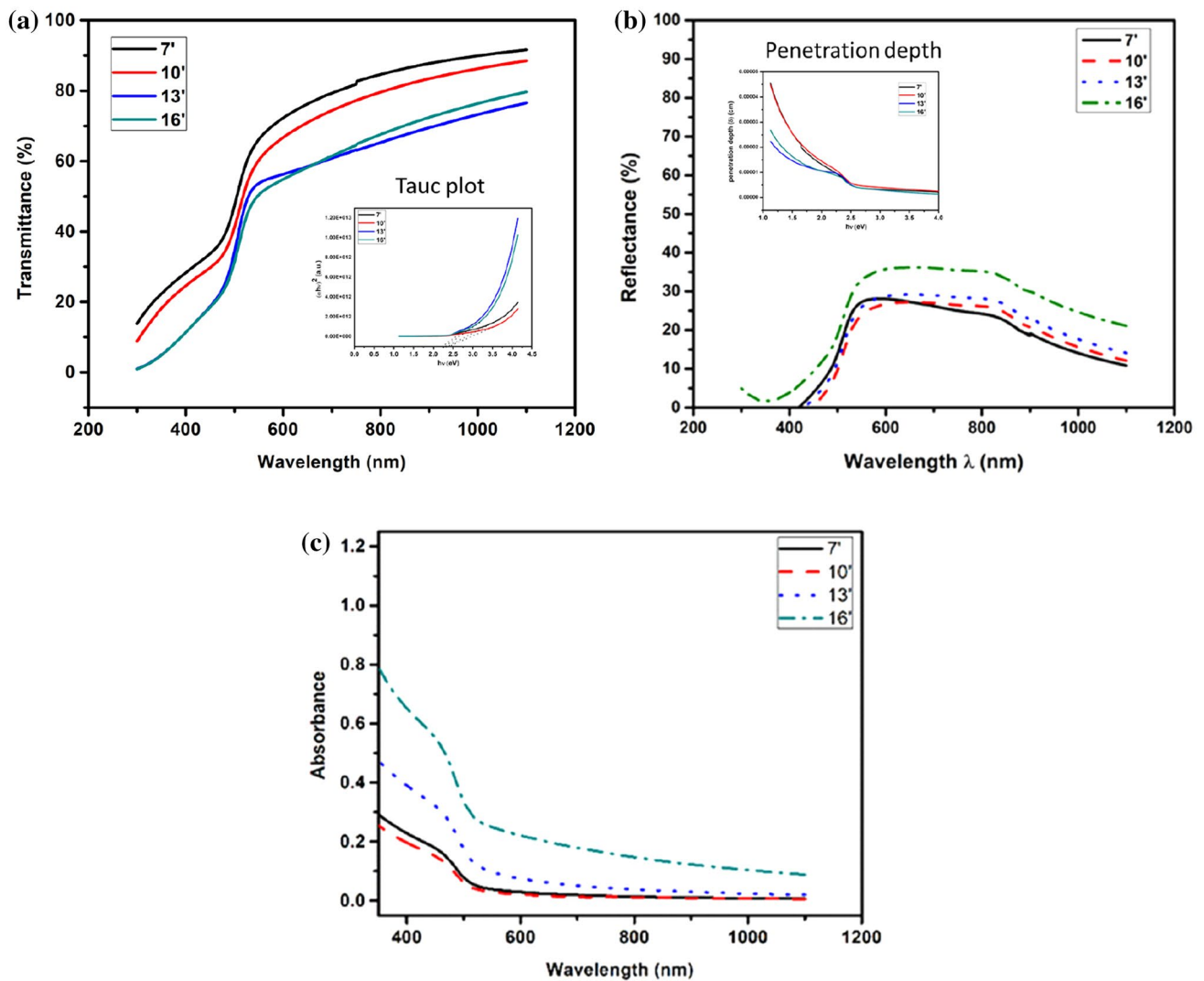


**Fig. 14** Plot of **a** Optical transmittance (inserted with Tauc plot), **b** reflectance (inserted with penetration depth curve), and **c** absorbance of CdS thin film deposited at 70 °C for different times

CdS films, transmission curves showed no fluctuations and wave-like patterns. The optical transmission was largest for the film deposited at 7 min, which was around 66% at 550 nm. The transmission value was decreased with increasing the deposition time. A similar pattern of the reflectance to that of transmittance was observed for the deposited films. The reflectance was 31% for the film deposited for 7 min at 550 nm.

Tauc plot (see in Fig. 14a) shows the schematic diagram between  $(\alpha h\nu)^2$  versus  $h\nu$  for  $n = 1/2$ . The band gap energy of CdS thin films was calculated by extrapolating the straight-line portion of the plot  $(\alpha h\nu)^2$  to energy axis and was found to be 2.30 eV (7 min), 2.33 eV (10 and 13 min), and 2.35 eV (16 min). The lowering of the band gap for 7 min may be due to the presence of impurity electronic levels in the forbidden gap [92]. The photon absorbed within the CdS thin

films generally depends upon the parameters like material quality, thickness, conductivity, and extinction coefficient. All the incident photon into the films is absorbed mostly in the spectral region of intense absorption and the remaining is reflected at the surface. The characteristic features like skin or penetration depth, optical conductivity are useful tools to understand the absorption nature of photons within the film. The photon current density decreases exponentially from the surface to the depth of the film due to properties like density, refractive index, morphology, and microstructure of samples. The thickness at which the photon density becomes  $1/e$  of the value at the surface of the film is given by penetration depth and is calculated mathematically by the reciprocal of the absorption coefficient ( $\alpha$ ). The dependence of penetration depth of CdS thin film on the incident photon energy is given in Fig. 14b. It was found that the penetration

depth was decreased as the photon energy increased for all the CdS samples. For a cut-off wavelength ( $\lambda = 550$  nm), the absorption effect was decreased and vanished after passing through more depth. The data revealed that the penetration depth is also related to transmittance values.

### 3.6.2 Process two

The transmittance of the CdS thin films deposited at various temperatures and times are shown in Fig. 15 and the data were studied in the wavelength ranging from 300 to 900 nm. The deposited thin films transmit the light more than 90% in the wavelength range from 600 to 800 nm. With these results of transmittance, there might be a high amount of photon energy passing through a buffer layer to the absorber layer in thin-film solar cells. Hence, a higher amount of energy can be absorbed, a large number of electron–hole pairs can be generated in an absorber layer, which increases the efficiency of solar cells.

The band gap energy of CdS thin films is the photon energy that can be calculated by extrapolating the straight-line part of the plot ( $\propto h\nu$ )<sup>2</sup> versus photon energy ( $h\nu$ ) to the energy axis (i.e., ( $\propto h\nu$ )<sup>2</sup> = 0). It is seen, from Fig. 15, that the value of  $E_g$  for CdS films prepared at different temperatures and times varies from 2.65 to 2.52 eV and 2.49 to 2.62 eV with increasing order, respectively. The band gap of CdS thin films calculated from Tauc relation was close to the 2.58 eV value showing films are stable as well as wurtzite crystal structure can be useful as a buffer layer in photovoltaic cells.

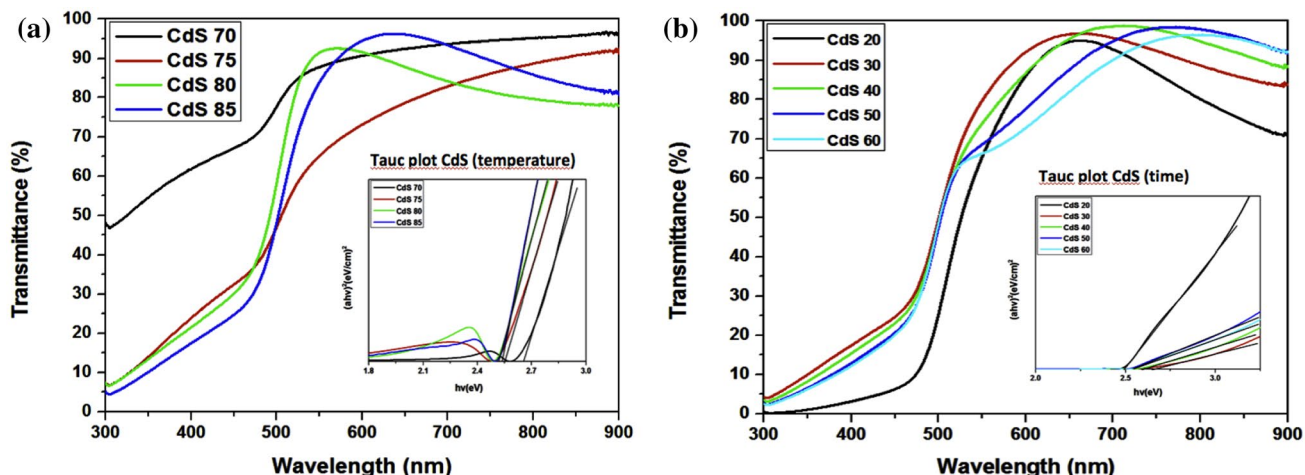


**Fig. 15** Transmittance of CdS thin films (inserted with band gap energy diagram) fabricated at different deposition **a** temperature and **b** time conditions

## 3.7 Photoluminescence studies

### 3.7.1 Process one

Photoluminescence (PL) studies give valuable information on the atomic constitution and the quality of the material. PL spectra of CdS thin films were recorded at ambient condition for CdS thin films deposited by CBD technique as shown in Fig. 16. For an excitation wavelength of 325 nm, the major emission peak was observed at a wavelength of 537 nm (2.30 eV) for the film deposited for 7 min. The slight shift in the emission peak was observed for the films deposited for 10, 13, and 16 min. The emission peaks were identified at 533, 531, and 530 nm for 10, 13, and 16 min, respectively. The emission peak at around energy value of 2.3 eV for all the

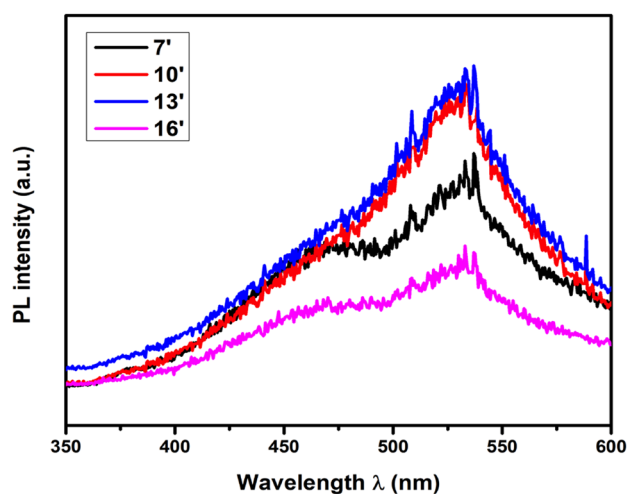


**Fig. 16** PL spectra of CdS thin film at 70 °C for different deposition times

deposited CdS thin films is due to the near band edge (NBE) emission arising due to the recombination of free excitons [93]. The emission peak position of the CdS thin film almost nearly matches the determined optical band gap values. The maximum PL was observed because the concentration of Cd vacancies acts as acceptors and the ground state is excited to the higher arbitrary level. The probability of this energy transfer process increases with a shorter donor–acceptor distance and hence luminescence decreases with increasing concentration.

### 3.7.2 Process two

The quality of films influenced by the factors such as impurities, defect centers, and recombination of surface states can be analyzed by PL studies. Furthermore, information involving different energy states lies between valence and conduction bands that are responsible for radiative recombination due to cadmium and/or sulfur defects are also achieved by PL studies. Figure 17a shows the PL spectra of CdS thin films deposited with various temperatures from 70 to 85 °C at constant time of 30 min and Fig. 17b represents with different times from 20 to 60 min at constant temperature condition (80 °C). For both deposition temperatures and time, there was one major peak in the ranging from 2.2 to 2.6 eV as shown in Fig. 17. The red emission (RE) band is located in the range 1.7–1.86 eV energy level, which is due to cadmium interstitial (i.e., sulfur vacancies) [94]. The yellow emission (YE) band, situated in the range of 2.04–2.11 eV, arises by cadmium vacancies ( $I_{cd}-V_{cd}$ ) defects [95]. The energy bandgap values between 2.40 to 2.60 eV in PL spectra is known as a green emission band that can be assigned

due to sulfur interstitials where electronic transitions take place from the conduction band to an acceptor level [96, 97]. In this study, the presence of GE band in the PL spectra verified the better crystallinity of material, decrease in the number of grain boundaries by enhancing the grain size as well as minimizing the density of native defects. In addition, there are several peaks located at 2.43, 2.47, and 2.58 eV ascribed to bound exciton for a mixture of cubic and hexagonal phases of CdS thin films. The PL intensity of CdS film decreases with the increase in the concentration of sulfur atoms (i.e., S/Cd ratio) that reduces the defect density [98, 99]. It is seen that the intensity of the band decreases in higher deposition time and temperature due to the increase in sulfur interstitials. The higher PL intensity of films may have the presence of recombination sites, impurities, as well as the non-homogenous distribution of atoms.

## 3.8 Electrical properties

### 3.8.1 Process one

The Hall effect Vander Pauw method estimated the high resistive values for the samples prepared by process one.

### 3.8.2 Process two

Conductivity, the degree of conduction of electricity, of the CdS thin films was estimated from the reciprocal of resistivity measurements. The main concerns of electrical measurements like Hall coefficient (type of semiconductors), conductivity, mobility, and carrier concentration of CdS thin films measured at room temperature and their co-relation

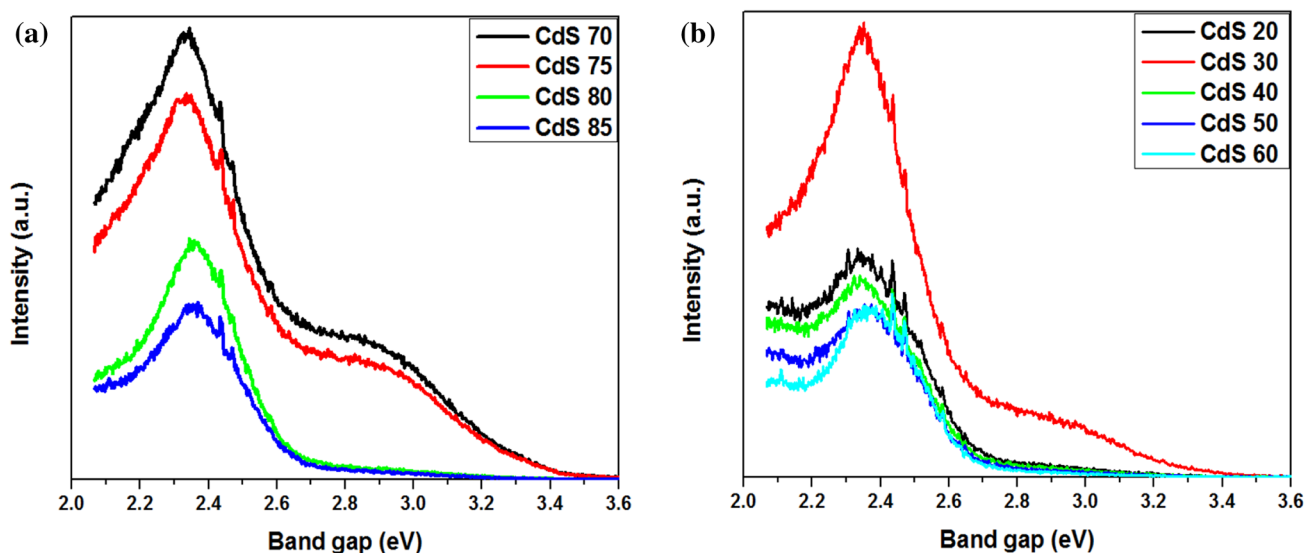


Fig. 17 PL spectra of CdS thin films at various deposition **a** temperatures and **b** times



**Table 8** Electrical properties of CdS thin films prepared by CBD method

Parameters Samples	Hall coefficient (cm <sup>3</sup> /C)	Conductivity ( $\sigma$ ) ( $\Omega^{-1}\text{cm}^{-1}$ )	Mobility ( $\mu$ ) (cm <sup>2</sup> /V-s)	Carrier concentration n (cm <sup>-3</sup> )
CdS 70 °C 30 min	–	–	–	–
CdS 75 °C 30 min	–	–	–	–
CdS 80 °C 30 min	– 329	5.16E–2	– 17	1.9E16
CdS 85 °C 30 min	– 75	8.00E–2	– 6	8.3E16
CdS 80 °C 20 min	– 13888	8.35E–3	– 116	4.5E14
CdS 80 °C 30 min	– 160	9.37E–2	– 15	3.9E16
CdS 80 °C 40 min	– 868	3.57E–2	– 31	7.2E15
CdS 80 °C 50 min	– 11160	6.63E–3	– 74	5.6E14
CdS 80 °C 60 min	– 625	2.56E–2	– 16	1.0E16

properties are shown in Table 8. The deposited films at higher temperatures have higher conductivity, which may be due to increasing thickness of films (i.e., few numbers of pinholes) where distributions of ions are uniform. The properties such as band gap narrowing, decrease in grain boundary density and dislocation density, and an increase in grain sizes of the films are due to the increase in carrier concentration [84]. The Hall-van der Pauw method could not calculate the electrical parameters of the CdS films deposited at lower temperature (less than 75 °C) showing more resistive due to the presence of pinholes inside the films. The n-type conducting nature of CdS thin films was verified by the presence of negative values of Hall coefficient. By doping impurities (i.e. Na, K) and by allowing cadmium interstitials or sulfur vacancies help to enhance the conductivity of CdS thin films [100]. When CdS thin film is used as a buffer layer in thin film solar cells, then the high value of conductivity of CdS film helps to separate the generated charge carriers effectively during photovoltaic energy conversion and consequently increases the efficiency of the solar cell.

## 4 Conclusions

CdS thin films were successfully synthesized over SLG substrates with different deposition parameters. An extra precursor material, i.e., ammonium acetate, was added on second process in order to study its effect on the properties of CdS thin films. The growth of the film depending

on the deposition parameters such as temperature, time, and concentration of precursors was observed clearly from the experiments. XRD results exhibited that both fabrication techniques gave a hexagonal crystal structure with a preferential orientation along (002) with a crystallite size varied from 20 to 40 nm. The appearance of the first LO at 305 cm<sup>-1</sup> and second LO at 605 cm<sup>-1</sup> verified the hexagonal structure of CdS thin films investigated from Raman spectroscopy. From the SEM analysis, uniform, smooth, dense film with less pinhole, spherical grains was observed in both the synthesis processes. An enhancement of the film surface atomic mobility was observed at higher deposition temperatures and times. RMS roughness, as determined by AFM measurements, of the CdS films was seen in the range of 5–11 nm showing grains are compact and uniformly distributed. The values of transmittance in the aforementioned CBD methods started to increase after 500 nm and demonstrated more than 70% of transmittance in the visible spectrum. The optical band gap, for better conditions, was found around 2.33 eV and 2.52 eV for process one and process two, respectively. From PL spectra, the energy band of films lies in between 2.4 and 2.6 eV, called green emission band; the peak intensity decreased with increase in deposition temperature and time revealing that the number of impurities, defect centers, and recombination of surface states decreases. Hall effect studies demonstrated that CdS thin films fabricated by process two were more conductive than CdS films by process one. Hence, CdS thin films deposited by process two, at temperature 80 °C for 30 min, were most suitable deposition condition as a buffer layer for thin-film solar cells.

**Acknowledgements** We wish to acknowledge the financial support from the project, Consejo Nacional de Ciencia y Tecnología-Secretaría de Energía (CONACyT—SENER)—263043. The authors A. Ashok and G. Regmi would like to thank CONACyT for the doctoral scholarship. We are also thankful to Jaime Vega Perez, Eduardo Pérez Garduño, Miguel A. Avendaño Ibarra, Norma Iris Gonzalez Garcia, Miguel Galvan Arellano, Francisco Alvarado Cesar, and Adolfo Távira Fuentes from section of solid-state electronics of Centro de Investigación y De Estudios Avanzados del Instituto Politécnico Nacional (CINVESTAV-IPN) for their technical help.

## References

1. A. Luque, S. Hegedus, *Handbook of Photovoltaic Science and Engineering*, (Wiley, Hoboken, 2011), pp. 11–41
2. A. Fahrenbruch, R. Bube, *Fundamentals of Solar cells: Photovoltaic Solar Energy Conversion*, (Elsevier, Amsterdam, 1983) pp. 1–23
3. V. Steinbach, F.W. Wellmer, *Sustainability* **2**, 1408 (2010)
4. A. Jager-Waldau, Snapshot of photovoltaics. *EPJ Photovolt.* **9**, 6 (2018)
5. H. Neumann, *Sol. Cells* **16**, 317 (1986)



6. B. Dimmler, CIGS and CdTe based thin film PV modules, (38th IEEE Photovoltaic Specialists Conference, 2012), pp. 002494–002499
7. G. Regmi, M. Rohini, P. Reyes-Figueroa, A. Maldonado, María De La Luz Olvera, S. Velumani, *J. Mater. Sci.* **29**, 15682 (2018)
8. M.M. de Wild-Scholten, *Sol. Energy Mater. Sol. Cells* **119**, 296 (2013)
9. K.K. Solar, Frontier, Solar Frontier achieves world record thin-film solar cell efficiency of 22.9%, press release, (2017)
10. C. Heske, D. Eich, R. Fink, E. Umbach, T. van Buuren, C. Bostedt, L.J. Terminello, S. Kakar, M.M. Grush, T.A. Callcott, F.J. Himpsel, D.L. Ederer, R.C.C. Perera, W. Riedl, F. Karg, *Appl. Phys. Lett.* **74**, 1451 (1999)
11. R.H. Bube, *Photoelectronic Properties of Semiconductors*, (Cambridge University Press, Cambridge, 1992) pp. 1–29
12. J. Sterner, J. Malmstrom, L. Stolt, J. Malmström, L. Stolt, *Prog. Photovolt. Res. Appl.* **13**, 179 (2005)
13. C. Platzer-Bjorkman, J. Kessler, L. Stolt, In 3rd World Conf. Photovolt. Energy Convers. **1**, 461 (2003)
14. A. Ennaoui, M. Weber, R. Scheer, H.J. Lewerenz, *Sol. Energy Mater. Sol. Cells* **54**, 277 (1998)
15. A.M. Chaparro, C. Maffiotte, M.T. Gutiérrez, J. Herrero, J. Klaer, K. Siemer, D. Bräuni, *Thin Solid Films* **387**, 104 (2001)
16. G. Gordillo, C. Calderón, *Sol. Energy Mater. Sol. Cells* **77**, 163 (2003)
17. N. Naghavi, S. Spiering, M. Powalla, B. Cavana, D. Lincot, *Prog. Photovolt. Res. Appl.* **11**, 437 (2003)
18. P. Genevee, A. Darga, C. Longeaud, D. Lincot, F. Donsanti, *J. Renew. Sustain. Energy* **7**, 013116 (2015)
19. R.A. Devi, M. Latha, S. Velumani, G. Oza, P. Reyes-Figueroa, M. Rohini, *J. Nanosci. Nanotechnol.* **15**, 8434 (2015)
20. P.K. Nair, J. Campos, M.T.S. Nair, *Semicond. Sci. Technol.* **3**, 134 (1998)
21. A. Dandia, V. Parewa, K.S. Rathore, *Catal. Commun.* **28**, 90 (2012)
22. N. Zhu, A. Zhang, P. He, Y. Fang, *Analyst* **128**, 260 (2003)
23. S.D. Naik, S.K. Apte, R.S. Sonawane, U.P. Mulik, *Pramana* **65**, 707 (2005)
24. R. Agarwal, C.J. Barrelet, C.M. Lieber, *Nano Lett.* **5**, 917 (2005)
25. J.B. Seon, S. Lee, J.M. Kim, H.D. Jeong, *Chem. Mater.* **21**, 604 (2009)
26. J. Zhang, D. Li, R. Chen, Q. Xiong, *Nature* **493**, 504 (2013)
27. A.A. Yadav, E.U. Masumdar, *J. Alloys Compd.* **509**, 5394 (2011)
28. X. Mathew, J.P. Enriquez, A. Romeo, A.N. Tiwari, *Sol. Energy* **77**, 831 (2004)
29. A. Ashok, J.S. Narro-Rios, O. Nwakanma, G. Regmi, F.A. Pulgarin-Agudelo, S. Velumani, 15th International Conference on Electrical Engineering, Computing Science and Automatic Control (CCE) IEEE 1, (2018)
30. G. Regmi, J.S. Narro-Rios, O. Nwakanma, A. Ashok, F.A. Pulgarin-Agudelo, S. Velumani 15th International Conference on Electrical Engineering, Computing Science and Automatic Control (CCE) IEEE 1, (2018)
31. B.J. Babu, S. Velumani, B.J. Simonds, R.K. Ahrenkiel, A. Kassiba, R. Asomoza, *Mater. Sci. Semicond. Process* **37**, 37 (2015)
32. B. Vidhya, S. Velumani, R. Asomoza, *J. Nanopart. Res.* **13**, 3033 (2011)
33. M. Latha, R.A. Devi, S. Velumani, G. Oza, P. Reyes-Figueroa, M. Rohini, J. Yi, *J. Nanosci. Nanotechnol.* **15**, 8388 (2015)
34. M. Rohini, P. Reyes, S. Velumani, M. Latha, I. Becerril-Juarez, R. Asomoza, *Mater. Sci. Semicond. Process.* **37**, 151 (2015)
35. B.J. Babu, S. Velumani, A. Kassiba, R. Asomoza, J.A. Chavez-Carvayar, J. Yi, *Mater. Chem. Phys.* **162**, 59 (2015)
36. M. Chandramohan, S. Velumani, T. Venkatachalam, *Mater. Sci. Eng. B* **174**, 205 (2010)
37. H. Moualkia, S. Hariech, M.S. Aida, N. Attaf, E.L. Laifa, *J. Phys. D* **42**, 135404 (2009)
38. P. Reyes, S. Velumani, *Mater. Sci. Eng. B* **177**, 1452 (2012)
39. T. Nakada, M. Mizutani, Y. Hagiwara, A. Kunioka, *Sol. Energy Mater. Sol. Cells.* **49**, 249 (1997)
40. P. Jackson, D. Hariskos, R. Wuerz, O. Kiowski, A. Bauer, T.M. Friedlmeier, M. Powalla, *Phys. Status Sol. Rapid Res. Lett.* **9**, 28 (2015)
41. C.T. Tsai, D.S. Chuu, G.L. Chen, S.L. Yang, *J. Appl. Phys.* **79**, 9105 (1996)
42. B.S. Moon, J.H. Lee, H. Jung, *Thin Solid Films* **511**, 299 (2006)
43. P.P. Sahay, R.K. Nath, S. Tewari, *Cryst. Res. Technol.* **42**, 275 (2007)
44. K. Sivaramamoorthy, S.A. Bahadur, M. Kottaisamy, K.R. Murali, *J. Alloys Compd.* **503**, 170 (2010)
45. D.W. Niles, H. Hochst, *Phys. Rev. B* **41**, 12710 (1990)
46. N.V. Hullavarad, S.S. Hullavard, *Photonics Nanostruct. Fundam. Appl.* **5**, 156 (2007)
47. J. Nishino, S. Chatani, Y. Uotani, Y. Nosaka, *J. Electroanal. Chem.* **473**, 217 (1999)
48. E. Fatas, R. Duo, P. Herrasti, F. Arjona, E. Garcia-Camarero, *J. Electrochem. Soc.* **131**, 2243 (1984)
49. S.A. Al-Kuhaimi, *Vacuum*, **51**, 349 (1998)
50. J. Patel, F. Mighri, A. Ajji, D. Tiwari, T.K. Chaudhari, *Appl. Phys. A* **117**, 1791 (2014)
51. M.A. Olopade, A.M. Awobode, O.E. Awe, T.I. Imalerio, *Int. J. Res. Rev. Appl. Sci.* **15**, 120 (2013)
52. A.A. Yadav, M.A. Barote, E.U. Masumdar, *Solid State Sci.* **12**, 1173 (2010)
53. A. Ashour, *Turk. J. Phys.* **27**, 551 (2003)
54. H. Uda, H. Yonezawa, Y. Ohtsubo, M. Kosaka, H. Sonumura, *Sol. Energy Mater. Sol. Cells* **75**, 219 (2003)
55. H.M. Pathan, C.D. Lokhande, *Bull. Mater. Sci.* **27**, 85 (2004)
56. Z. Rabeel, M. Abbas, M. Basit, N.A. Shah, I. Ahmad, *J. Adv. Nanomater.* **2**, 113 (2017)
57. J.P. Enriquez, X. Mathew, *Sol. Energy Mater. Sol. Cells* **76**, 313 (2003)
58. R. Hunger, M.V. Lebedev, K. Sakurai, T. Schulmeyer, T. Mayer, A. S. Klein, W. Niki, Jaegermann, *Thin Solid Films* **515**, 6112 (2007)
59. D.C. Reynolds, G. Leies, L.L. Antes, R.E. Marburger, *Phys. Rev.* **96**, 533 (1954)
60. P.K. Nair, M.T.S. Nair, V.M. Garcia, O.L. Arenas, Y. Pena, A. Castillo, I.T. Ayala, *Sol. Energy Mater. Sol. Cells* **52**, 313 (1998)
61. J. Emerson-Reynolds, *J. Chem. Soc.* **45**, 162 (1884)
62. H. Khallaf, I.O. Oladeji, G. Chai, L. Chow, *Thin Solid Films* **516**, 7306 (2008)
63. F. Ouachtari, A. Rmili, B. Elidrissi, A. Bouaoud, H. Erguig, P. Elies, *J. Mod. Phys.* **2**, 1073 (2011)
64. G. Hodes, *Chemical Solution Deposition of Semiconductor Films* (CRC Press, Boca Raton, 2002), pp. 1–14
65. A.A. Uritskaya, G.A. Kitaev, N.S. Belova, *RusS. J. Appl. Chem.* **75**, 846 (2002)
66. N.G. Dhere, D.L. Waterhouse, K.B. Sundaram, O. Melendez, N.R. Parikh, B. Patnaik, *J. Mater. Sci.* **6**, 52 (1995)
67. S. Hariech, M.S. Aida, J. Bougdira, M. Belmahi, G. Medjahdi, D. Genève, N. Attaf, H. Rinnert, *J. Semicond.* **39**, 034004 (2018)
68. E. Çetinörgü, C. Gümüş, R. Esen, *Thin Solid Films* **515**, 1688 (2006)
69. L. Wenyi, C. Xun, C. Qiulong, Z. Zhibin, *Mater. Lett.* **59**, 1 (2005)
70. M. Cao, Y. Sun, J. WU, X. Chen, N. Dai, *J. Alloys Compd.* **508**, 297 (2010)

71. O. Vigil-Galán, F.A. Pulgarín, F. Cruz-Gandarilla, M. Courel, G. Villarreal-Ruiz, Y. Sánchez, D. Jiménez-Olarte, *Mater. Des.* **99**, 254 (2016)
72. D. Abou-Ras, G. Kostorz, A. Romeo, D. Rudmann, A.N. Tiwari, *Thin Solid Films* **481**, 118 (2005)
73. K. Orgassa, U. Rau, Q. Nguyen, H.W. Schock, J.H. Werner, *Prog. Photovolt. Res. Appl.* **10**, 457 (2002)
74. F. Lisco, P.M. Kaminski, A. Abbas, K. Bass, J.W. Bowers, G. Claudio, M. Losurdo, J.M. Walls, *J. Thin Solid Films* **582**, 323 (2015)
75. K.S. Ramaiah, R.D. Pilkington, A.E. Hill, R.D. Tomlinson, A.K. Bhatnagar, *Mater. Chem. Phys.* **68**, 22 (2001)
76. A.J. Khimani, S.H. Chaki, T.J. Malek, J.P. Tailor, S.M. Chauhan, M.P. Deshpande, *Mater. Res. Express* **5**, 036406 (2018)
77. R. Sathishkumar, E. Devakirubai, A. David, S. Tamilselvan, S. Nithiyantham, *Mater. Focus* **6**, 41 (2017)
78. J. Trajić, M. Gilić, N. Romčević, M. Romčević, G. Stanišić, B. Hadžić, *Sci. Sinter.* **47**, 145 (2015)
79. J.H. Kwon, J.S. Ahn, H. Yang, *Curr. Appl. Phys.* **13**, 84 (2013)
80. S.R. Meher, D.K. Kaushik, A. Subrahmanyam, *J. Mater. Sci. Mater. Electron.* **28**, 6033 (2017)
81. S. Aksay, M. Polat, T. Ozer, S. Kose, G. Gurbuz, *Appl. Surf. Sci.* **257**, 10072 (2011)
82. S. Aksay, *A Appl. Sci. Eng.* **19**, 1013 (2018)
83. C.C. Bijumon, V.S. Kumar, *Int. J. Phys. Res.* **6**, 31 (2016)
84. M. Oztas, M. Bedir, M.Y. Hacıbrahim, Y. Ozdemir, *Nanomed. Nanotechnol.* **3**, 000130 (2018)
85. M.A. Martinez, C. Guillen, J. Herrero, *Appl. Surf. Sci.* **136**, 8 (1998)
86. A.A. Prema, R.J. Xavier, P.A. Sahayaraj, C. Pragathiswaran, *Der. Pharma Chem.* **8**, 96 (2016)
87. K.K. Nanda, S.N. Sahu, *Appl. Surface Sci.* **119**, 50 (1997)
88. E. Yücel, N. Güler, Y. Yücel, *J. Alloys Compd.* **589**, 207 (2014)
89. S. Kahraman, H.M. Çakmak, S. Çetinkaya, H.A. Çetinkara, H.S. Güder, *J. Phys. Chem. Solids* **74**, 565 (2013)
90. H. Moualkia, S. Hariech, M.S. Aida, N. Attaf, E.L. Aifa, *J. Phys. D* **42**, 135404 (2009)
91. H. Fritzsche, *Sol. Energy Mater.* **3**, 447 (1980)
92. H. Metin, R. Esen, *J. Cryst. Growth* **258**, 141 (2003)
93. A.S. Lahewil, Y. Al-Douri, U. Hashim, N.M. Ahmed, *Sol. Energy* **86**, 3234 (2012)
94. A. Palafox, G. Romero-Paredes, A. Maldonado, R. Asomoza, D.R. Acosta, J. Palacios-Gómez, *Solar Energy Mater. Sol. Cells* **55**, 31 (1998)
95. B.A. Kulp, R.H. Kelley, *J. Appl. Phys.* **31**, 1057 (1960)
96. H. Ariza-Calderon, R. Lozada-Morales, O. Zelaya-Angel, J.G. Mendoza-Alvarez, *J. Vac. Sci. Technol. A* **14**, 2480 (1996)
97. J. Aguilar-Hernandez, G. Contreras-Puentes, A. Morales-Acevedo, O. Vigil-Galan, *Semicond. Sci. Technol.* **18**, 111 (2003)
98. F. Gemain, I. Robin, S. Renet, *Phys. Status Solid* **9**, 1740 (2012)
99. P.S. Suryavanshi, C.J. Panchal, *J. Nano Electron. Phys.* **10**, 02012 (2018)
100. R. Hill, *Solid State Electron. Devices* **2**, 49 (1978)

**Publisher's Note** Springer Nature remains neutral with regard to jurisdictional claims in published maps and institutional affiliations.